



Deposited via The University of Leeds.

White Rose Research Online URL for this paper:

<https://eprints.whiterose.ac.uk/id/eprint/137796/>

Version: Accepted Version

Article:

Luo, M, Glover, PWJ and Pan, H (2019) A reassessment of the stress and natural fracture orientations from analysis of image logs in the Chinese Continental Scientific Drilling Program borehole at Donghai county, Jiangsu province, China. *Journal of Asian Earth Sciences*, 169. pp. 11-20. ISSN: 1367-9120

<https://doi.org/10.1016/j.jseaes.2018.10.014>

© 2018 Elsevier Ltd. This manuscript version is made available under the CC-BY-NC-ND 4.0 license <http://creativecommons.org/licenses/by-nc-nd/4.0/>.

Reuse

This article is distributed under the terms of the Creative Commons Attribution-NonCommercial-NoDerivs (CC BY-NC-ND) licence. This licence only allows you to download this work and share it with others as long as you credit the authors, but you can't change the article in any way or use it commercially. More information and the full terms of the licence here: <https://creativecommons.org/licenses/>

Takedown

If you consider content in White Rose Research Online to be in breach of UK law, please notify us by emailing eprints@whiterose.ac.uk including the URL of the record and the reason for the withdrawal request.

1 **A reassessment of the stress and natural fracture orientations from analysis**
2 **of image logs in the Chinese Continental Scientific Drilling Program**
3 **borehole at Donghai county, Jiangsu province, China**

4

5 Miao Luo^{a, b*}, Paul W.J. Glover^b, Heping Pan^a

6

7 ^aHubei Subsurface Multi-scale Imaging Key Lab, Institute of Geophysics and Geomatics,

8 China University of Geosciences, Wuhan 430074, China

9 ^bSchool of Earth and Environment, University of Leeds, Leeds LS2 9JT, UK

10

11

12

13

14

15

16

17

18

19

20

21

22

23

24

Abstract

25 The Chinese Continental Scientific Drilling (CCSD) project has drilled a 5100 m deep
26 research borehole in the Sulu ultra-high pressure (UHP) metamorphic belt, eastern China. The
27 UHP metamorphic belt is thought to be a product of continent-continent collision and has
28 consequently experienced very intensive structural deformation. Based on a more complete
29 well log data set of CCSD borehole, we can have a more detailed and reliable study on the
30 structure features of borehole wall and other rock physical properties than a previous study
31 published in 2009. Abundant data related to borehole breakouts (BOs), drilling induced
32 tensile fractures (DITFs) and natural fractures were collected from the image logs. The BO
33 and DITF data indicate that the average direction of the maximum horizontal principal stress
34 (S_H) of the CCSD borehole site is about 79.2° which is consistent with the convergent
35 direction (E-W) of the Pacific Sea Plate with respect to the Eurasian Plate. Analysis of DITFs
36 indicated that in the case of the CCSD borehole, axial drilling induced tensile fractures
37 (ADITFs) occur occasionally in the upper section (0-2300 m) of the borehole with low
38 dipping angle ($0-10^\circ$), while transverse drilling induced tensile fractures (TDITFs) occur
39 significantly in the lower section (3800-5000 m) with high dipping angle ($10-30^\circ$). The
40 natural fracture distribution at depth in the metamorphic rocks of the CCSD borehole
41 indicates that (1) the failure strength of rocks and borehole depth are two factors that affects
42 natural fracture frequency, (2) most of the dip azimuth of natural fractures is consistent with
43 the dip azimuth of foliations observed in the core, (3) the development of most of the natural
44 fractures probably was dominated by the development of foliations, and both the natural

45 fractures and foliations developed in response to the subduction and exhumation of the Sulu
46 terrene.

47 **Keywords:** continental deep drilling; image logs; stress orientation; borehole breakout;
48 drilling induced tensile fracture; natural fracture distribution

49 **1. Introduction**

50 Knowledge of the in-situ stress state of the formation and Earth crust is very important
51 for the study of borehole stability (Zoback et al., 2003; Zhang et al., 2009; Tingay et al., 2009;
52 Zhang, 2013), hydraulic fracture stimulation (Haimson and Fairhurst, 1967; Maxwell et al.,
53 2009; Davies et al., 2012; Schmitt and Haimson, 2016; Rajabi et al., 2017), well path design
54 (Goodman and Connolly, 2007), water flooding (Nelson, 2005), and earthquake fault system
55 evolution (Stein, 1999; Sandiford, 2003; Sibson et al, 2011; Nie et al, 2013).

56 When studying the stress field of the Earth crust, researchers often assume an
57 Andersonian (1951) state of stress with that the direction of one of the principal stresses is
58 vertical, so the three orthogonal principal stresses are: (i) a vertical stress (S_V), (ii) a maximum
59 (S_H) and (iii) a minimum horizontal principal stress (S_h) (Schmitt et al., 2012). The direction
60 of S_H is a key parameter in the study of the present formation stress and regional stress field.
61 Under the impact of contemporary stress field, borehole breakouts (BOs) occur when the
62 hoop stress around the borehole wall exceeds the compressive strength of the borehole wall
63 rocks (Bell and Gough, 1979; Zoback et al, 1985) (Fig. 1a). Meanwhile, drilling induced
64 tensile fractures (DITFs) occur when the hoop stress around the borehole wall exceeds that
65 required to cause tensile failure of the borehole wall (Fig. 1a). A great number of
66 investigations have shown that the orientation of BOs indicates the direction of the S_h and that

67 of DITFs indicates the direction of the S_H for a vertical or near-vertical well within an
68 Andersonian stress state (Fig. 1b) (Bell and Gough, 1979; Gough and Bell, 1982; Blumling et
69 al., 1983; Plumb and Hickman, 1985; Hickman et al., 1985; Zoback et al., 1985; Haimson and
70 Herrick, 1986; Vernik and Zoback, 1992; Aadnøy and Bell, 1998; Nelson, et al., 2005).
71 Subsequently, borehole image logs have been widely used to identify BOs and DITFs that are
72 related to the in-situ S_H and ascertain the S_H direction (Wu, et al., 2007; Tingay et al., 2008;
73 Rajabi, et al., 2010; Lin et al. 2010; Nie, et al., 2013).

74 Cui et al. (2009) has studied the present tectonic stress state of the Chinese Continental
75 Scientific Drilling (CCSD) wellbore site by using borehole cross-section data collected from
76 acoustic image logs. Their study indicates that the direction of the S_H of the CCSD wellbore
77 site is $49.5 \pm 3.5^\circ$. However, the world stress map indicates that the direction of the S_H at the
78 CCSD wellbore site is close to 80° . Thus, it is necessary to carry out more work at this
79 wellbore site.

80 In this study, we use both resistivity and ultrasonic image logs to obtain the BO and DITF
81 data and fracture distribution of the CCSD borehole, and then calculate the direction of the S_H
82 in the CCSD borehole in its present stress state. The fracture distribution in the borehole is
83 probably related to the in-situ lithology and its structure, which are, in turn, related to the
84 subduction and exhumation process of the Sulu ultra-high pressure metamorphic (UHPM)
85 belt and can be used to study the evolution of the Sulu UHPM belt.

86 **2. Geological setting**

87 From 2001 to 2005 the Chinese government carried out a Chinese Continental Scientific
88 Drilling (CCSD) project to drill a vertical borehole in the southern part of the Sulu ultra-high

89 pressure metamorphic (UHPM) belt (N34°25', E118°40'), about 30 km east of the Tan-Lu
90 fault and 17 km southwest of Donghai County, as shown in Fig. 2.

91 The Dabie-Sulu UHPM belt is the largest recognized UHPM belts in the world. It has
92 become an ideal geological area for studying ultra-high pressure (UHP) metamorphism and
93 geodynamic mechanisms of continental subduction and exhumation since the discovery of
94 coesite-bearing eclogites (Okey et al., 1989; Wang et al., 1989) and diamond-bearing
95 eclogites (Xu et al., 1992). The Dabie-Sulu UHPM belt was formed by the Triassic collision
96 of the Sino-Korean and Yangtze craton with the peak metamorphic age of 220-245 Ma (Ames
97 et al., 1996; Hacker et al., 1998; Rowley et al., 1997). The UHPM rocks of the Dabie-Sulu
98 metamorphic belt have been subducted to at least 100 km and have experienced UHP
99 metamorphism before being rapidly exhumed from mantle depths and back to the surface.

100 The Sulu UHPM belt is commonly considered to be the eastern extension of the
101 Qinling-Dabie orogen. It is separated from the Sino-Korean craton to the NW by the
102 Yantai-Qingdao-Wulian Fault (YQWF), and the Yangtze craton to the SE by the
103 Jiashan-Xiangshui Fault (JXF). The Sulu terrane consists of two metamorphic units: the
104 northern UHPM belt and the southern high-pressure metamorphic belt (Zhang et al., 1995)
105 (Fig. 2).

106 The principal lithologies of the CCSD borehole include orthogneiss, paragneiss, eclogite,
107 and amphibolite together with minor amounts of ultramafic rock (Fig. 3). A detailed
108 description of the lithology and petrology is given by Liu et al. (2004).

109 The crystalline rocks of the CCSD borehole are hard and non-permeable, and
110 consequently the borehole shape varies little due to interactions between the drilling bit, the

111 drilling mud and the various lithologies through which the hole passes. The stability of the
112 borehole wall depends more on the formation stress and the development of fracture zones.

113 From a global point of view, the study area is located at the east part of the Eurasian Plate
114 (Fig. 2). Taking the Eurasian Plate as a reference, the Pacific Plate moves towards the WNW
115 and the Philippine Sea Plate moves towards the NW at present (Zhou and Ding, 1995; Kimura
116 et al., 2009). The east part of the Eurasian Plate is undergoing a strong compressive stress
117 field. Therefore, the CCSD borehole provides a very good opportunity to study the stress state
118 of the east part of the Eurasian Plate.

119 **3. Methodology**

120 ***3.1. Image log data acquisition***

121 The CCSD project carried out rigorous drilling and logging programme, and obtained a
122 large amount of high-quality core and well log data which provides us with an excellent
123 opportunity to study the fracture distribution in the borehole and the in-situ stress state of the
124 borehole site. The well log data of the CCSD borehole were acquired by the ECLIPS-5700
125 image logging system of Baker Hughes and the MAX-500 image logging system of
126 Schlumberger. Fig. 3 shows some conventional logs, such as gamma ray (GR), acoustic
127 velocity (V_P), density (DEN), deep resistivity (RD) and caliper (CAL). The images of the
128 CCSD borehole wall were obtained by resistivity and ultrasonic image logging tools. All the
129 logging tools were calibrated regularly to ensure its accuracy. Both the resistivity and
130 ultrasonic image logging tools contain orientation measurement device which can record the
131 azimuth of the tool in real time and output the unrolled pseudo-image of the borehole wall
132 oriented to the geographic north (0°) (Fig. 4).

133 The resistivity image tools are pad tools that measure the formation micro resistivity
134 directly through an array of resistivity buttons mounted on pads that are pressed against the
135 borehole wall (Ekstrom et al, 1987). For the Schlumberger Fullbore Formation MicroImager
136 (FMI): vertical resolution: 5 mm; vertical sampling: 0.25 mm; depth of investigation: 76 mm
137 (Schlumberger, Ltd., 1994).

138 The ultrasonic imaging tools send sound pulses out to the formation by a transducer and
139 measure both the amplitude and the travel time of the returning signals reflected by the
140 borehole wall. The ultrasonic transducer can rotate continually and make 360° scanning. For
141 the Schlumberger Ultra-Sonic Borehole Imager: azimuthal resolution: 2°; vertical resolution
142 from 0.5 mm to 25.4 mm depending on pulse frequency (500 to 250 kHz); depth of
143 investigation: 0 (Gaillot, et al., 2007).

144 The ultrasonic imaging tools can perform well in both oil-based and water-based mud,
145 but the resistivity imaging tools only in water-based (conductive) mud. In addition,
146 ultrasonic image logs could be easily affected by borehole roughness or washouts.

147 ***3.2. Borehole breakouts and drilling induced tensile fractures***

148 With the resistivity and ultrasonic (amplitude) image logs, we can identify borehole wall
149 breakouts (BOs), drilling induced tensile fractures (DITFs) and natural fractures (NFs) in the
150 CCSD borehole (Fig. 4).

151 Previous studies proved that drilling induced tensile fractures (DITFs) fall into two types:
152 axial (vertical) drilling induced tensile fractures (ADITFs) and transverse drilling induced
153 tensile fractures (TDITFs) (Aadnøy and Bell, 1998; Brudy and Zoback, 1999). ADITFs
154 usually appear in vertical wells (the borehole axis is parallel to a principal stress), while

155 TDITFs usually occur in dipping wells (the borehole trajectory does not lie along a principal
156 stress direction) (Zoback, 2007, Schmitt et al., 2012).

157 In Fig. 4a, the two vertical dark bands on the image with a difference in their direction of
158 180 degree correspond to the borehole wall breakouts (BOs). In Fig. 4b, the two near-vertical
159 fractures apart 180 degree are axial drilling induced tensile fractures (ADITFs). In Fig. 4c, the
160 two groups of short fractures apart 180 degree with en-echelon structure are transverse
161 drilling induced tensile fractures (TDITFs).

162 For a vertical well, the direction of S_H is perpendicular to that of the BO and parallel to
163 that of the DITF (Zoback, 2007, Schmitt et al., 2012; Rajabi et al., 2017). Therefore, we can
164 determine the direction of S_H of the drilling site of the CCSD borehole by studying the
165 azimuthal direction of BOs and DITFs in the borehole.

166 ***3.3. Nature fractures and foliations***

167 Natural fractures and foliations usually appear as sinusoidal stripes on the resistivity and
168 ultrasonic image logs (Rider, 1996; Glover and Bormann, 2007; Serra, 2008).

169 In Fig. 5, both the resistivity and ultrasonic image logs present a dark quasi-sinusoidal
170 stripe which indicates there is a natural fracture at 232 m of the CCSD borehole. The dip
171 azimuth can be inferred from the lowest point of the quasi-sinusoidal stripe. In our case, the
172 dip azimuth is measured clockwise looking down the borehole from the geographic north.
173 Consequently, the dip azimuth of the fracture in Fig. 5 is approximately 200°.

174 Foliation in geology refers to repetitive layering in metamorphic rocks. It is caused by
175 shearing forces (pressures pushing different sections of the rock in different directions), or
176 differential pressure (higher pressure from one direction than in others) (Stephen, 2009).

177 Foliations can induce the development of natural fractures, so there are lots of natural
178 fractures parallel to the foliations (Massiot et al., 2018).

179 In Fig. 6, serial parallel dark and bright stripes on the FMI image indicate foliations. The
180 foliations display more crowded and continuous parallel structures than the natural fractures.
181 Furthermore, the foliations usually do not have very high resistivity and ultrasonic amplitude
182 contrast and display very weak logging anomaly and can only be observed sometimes on the
183 image logs. Due to the limitation of the logging tools' resolution, we cannot observe foliations
184 in most of the image logs of the CCSD borehole. Therefore, the studies of foliations usually
185 depend on the core. However, the natural fractures usually display lower resistivity and sonic
186 reflection amplitude than the surrounding rocks, so they have obvious features on both
187 resistivity and ultrasonic image logs and are relatively easy to be identified.

188 With the assistance of high-quality image logs and conventional well logs, the azimuth
189 and depth of cores can be restored (Fig. 5 and Fig. 6). Then, the true attitude information of
190 planar and linear structures on the cores can be obtained, which makes the core more valuable.
191 Conversely, the core images can be used to check the resolution and quality of the image logs.

192 **4. Results and discussion**

193 ***4.1. Orientation of the present S_H***

194 Analysis of the Formation Micro-resistivity Image (FMI) and Ultra-Sonic Image (USI)
195 logs from the CCSD borehole has allowed us to recognize 206 occurrences of breakout (BO)
196 and 26 occurrences of drilling induced tensile fracture (DITF). Fig. 7a and b show the
197 orientation distribution of BO and DITF with the depth in the CCSD borehole, while Fig. 7c
198 shows the orientation of S_H derived from the orientation of BO and DITF, respectively.

199 The azimuthal direction of most BOs (θ_{BO}) ranges from 150 to 180° with an arithmetic
200 mean of $\theta_{BO}= 168.6^\circ$ and a standard deviation of $\sigma_{\theta_{BO}}=17.9^\circ$. The azimuthal direction of most
201 DITFs (θ_{DITF}) ranges from 80° to 90° with an arithmetic mean of $\theta_{DITF}=83.3^\circ$ and a standard
202 deviation of $\sigma_{\theta_{DITF}}=12.3^\circ$. Consequently, the arithmetic mean of the azimuthal direction of S_H
203 θ_{HB} and θ_{HD} for values derived from BOs and DITFs, respectively, are $78.6\pm 17.9^\circ$ and
204 $83.3\pm 12.3^\circ$. It is clear that the azimuthal directions of S_H derived from BOs and DITFs
205 overlap significantly. In fact an unpaired t-test taking into account arithmetic means, standard
206 deviations and the number of samples in each set shows there to be no statistical difference
207 between them. The calculated *P*-value was 0.09 (or 9%), which is greater than 0.05 (5%), the
208 common threshold for considering 2 populations to be different. Accordingly, we can justify
209 taking the arithmetic mean of data for both BOs and DITFs to give a final value of $\theta_{SH} =$
210 $79.2\pm 17.4^\circ$. This degree of error classifies the overall azimuthal direction of horizontal
211 principle stress results presented in this work as having ‘Quality B’, according to world stress
212 map guidelines (Heidbach et al., 2016) while the individual results from BOs and DITFs,
213 have ‘Quality A’ and ‘Quality B’, respectively.

214 Our result ($\theta_{SH}= 79.2\pm 17.4^\circ$) agrees with most of the data from the adjacent areas, as
215 shown in Fig. 8, and is close to the E-W convergence direction between the Eurasian Plate
216 and the Pacific Plate (Fig. 1). Feng et al. (2017) studied the recent tectonic stress field at the
217 shallow earth's crust near the Tan-Lu fault zone. Their work indicted that the orientation of
218 the principal compressive stress of the present tectonic stress field near the CCSD borehole
219 area is N70°E which is close to our results.

220 The value we have calculated, however, is considerably different from the value of

221 $\theta_{SH}=49.5\pm 3.5^\circ$ reported by [Cui et al. \(2009\)](#). Application of an unpaired t-test to the combined
222 232 BO and DITF data from this work and the 143 well bore breakouts from [Cui et al. \(2009\)](#)
223 provides $P<0.0001$, indicating that there is less than a 0.1% chance of the two studies being in
224 agreement. This apparent variance clearly needs to be understood.

225 We have checked the causes of the difference between our results and that of [Cui et al.](#)
226 [\(2009\)](#). The study of [Cui et al. \(2009\)](#) used 143 borehole cross-sections collected from the raw
227 data of ultrasonic image logs which had not been processed, and only analysed well bore
228 breakouts. Furthermore, selected depths were chosen at random for the recognition, or not, of
229 borehole breakouts. By contrast, we have processed and analysed all of our image logs to
230 provide (i) cleaner images which will reduce or eliminate some errors caused by reading
231 unprocessed image log data, and (ii) a continuous coverage for the recognition of borehole
232 breakouts and DITFs over the whole depth range of the data. In our case, we identified BOs
233 using both resistivity image logs and ultrasonic image logs, leading to a more robust and
234 reliable identification of well bore breakouts. Not only we have recognised 206 occurrences
235 of well bore breakouts, but we also obtained 26 occurrences of DITF, which have been
236 analysed independently, and as we have noted above agree very well with the well for
237 breakout data. Consequently, this paper implements information from 232 orientable events in
238 the borehole compared to 143 for [Cui et al. \(2009\)](#), i.e., 89 more. Consequently, we attribute
239 the difference in our results compared to previous studies to our use of a greater number of
240 orientation data, obtained from multiple events (BO and DITF) using two different types of
241 fully processed image logs.

242 Axial drilling induced tensile fractures (ADITFs) and transverse drilling induced tensile
243 fractures (TDITFs) are commonly encountered in image logs. [Aadnøy and Bell \(1998\)](#) gave a
244 detailed classification of the borehole wall fractures and explained their origin. Fig. 7b shows
245 that in the case of the CCSD borehole, ADITFs occur occasionally in the upper section
246 (0-2300 m) of the borehole, while TDITFs occur significantly in the lower section (3800-5000

247 m). Fig. 7e shows that the deviation of the upper section (0-2300 m) of the borehole is
248 restricted to the range 0-10°, while that of the lower section (3800-5000 m) is greater, in the
249 range 10-30°.

250 It has already been recognised that ADITFs usually develop in vertical and slightly
251 dipping wells while TDITFs tend to occur in more deviated wells (Aadnøy and Bell, 1998;
252 Brudy and Zoback, 1999; Zoback, 2007, Schmitt et al., 2012). While we are disadvantaged by
253 a lack of data in the 3000-3600 m range, combining the results from Fig. 3b and e, suggests
254 that we can define a critical deviation angle below which ADITFs are more likely to occur
255 and above which TDITFs are more likely to occur. For the CCSD borehole, the critical
256 deviation angle seems to be approximately 10°.

257 **4.2. Magnitude of formation stress**

258 Within an Andersonian stress state, the direction of one of the principal stresses is vertical
259 because the surface is a free boundary and the gravitational acceleration is directed
260 downwards. The magnitude of the vertical stress (S_V) can be calculate by the equation

$$S_V(h) = \int_0^h \rho(h)gdh \quad (1)$$

261 where h denotes the borehole depth, g denotes the gravitational acceleration, ρ denotes the
262 density of rocks.

263 Fig. 7f displays the magnitudes of S_V , S_H and S_h versus depth. The magnitude of S_V was
264 calculated by density log. According to the stress state around the borehole and
265 Navier–Coulomb criterion, Zoback et al. (1985) developed two equations to estimate the
266 magnitudes of S_H and S_h based on the rock strength parameters and borehole breakout
267 geometry, Cui et al. (2009) employed the two equations and calculated the magnitudes of S_H

268 and S_h by core mechanical tests and borehole cross section data which derived from the
269 ultrasonic image logs. The magnitude relationship ($S_H > S_V > S_h$) of the three principal stresses
270 indicates that the regional stress field around the CCSD borehole is in a strike slip regime.
271 This is consistent with the previous study (Wan, et al., 1996; Zhu, et al., 2004, Deng, et al.,
272 2013).

273 *4.3. Distribution of fracture dip azimuth and frequency*

274 Numerous natural fractures are observed from the image logs of the CCSD borehole. Fig.
275 9a shows the distribution of the dip azimuth of natural fractures encountered by the borehole.
276 Fig. 9b indicates that the fracture frequency of the 0-3000 m interval is greater than that of the
277 3600-5000 m interval, so the depth can be a potential factor that affects fracture frequency. In
278 addition, the depth intervals (e.g. 1180-1220 m, 2200-2300 m) with very high fracture
279 frequency occur in paragneiss and orthogneiss. We infer that this is attributed to the
280 low-density and low-uniaxial failure strength of gneiss. The average density of gneiss and
281 eclogite are 2.6 and 3.5 g/cm³, respectively (Sun et al., 2012). The density log also showed
282 that the density of the 0-3000 m interval is greater than that of the 3000-5000 m interval (Fig.
283 3). The average uniaxial failure strengths of gneiss and eclogite are 110.03 and 143.47 MPa,
284 respectively (Cui et al., 2009).

285 To study the variation of fracture dip azimuth, we have split the well into 8 depth
286 intervals (Table 1). These intervals are the same as used by Xu et al. (2009) when they
287 divided the CCSD borehole into 6 big ‘petro-structure’ units according to the lithology and
288 the petrophysical properties of the core before reporting the dip azimuth of foliation of each
289 unit.

290 We have analyzed the dip azimuth of natural fractures for each of these 8 petrofacies
291 units, and shown it as rose diagrams in Fig. 10, noting that image data was missing in the
292 depth range 3000 to 3600 m, where no analysis could be carried out. Most of the depth ranges
293 exhibit a similar dip azimuth of natural fractures as can be seen in Fig. 10. Table 1 indicate
294 that the dip azimuth of natural fractures is similar with that of the foliations except unit D. Fig.
295 10g indicates that the dip azimuth of natural fractures is about 200° in the depth range
296 3623-5000 m, but Fig. 11h indicates that the dip azimuth of foliations is about 110° in the
297 depth range 3225-5158 m. The lithology of 3623-5000 m interval is mainly composed of
298 orthogneiss. Overall, we can conclude that the foliation direction could affect the
299 development of natural fractures greatly in our study borehole and most of the natural
300 fractures probably develop from the foliations (earlier ductile deformation) of the UHPM
301 rocks.

302 The study of [Xu et al. \(2009\)](#) showed that the forming of foliations with a dip azimuth of
303 $110\pm 10^\circ$ is the result of the subduction and exhumation of the Sulu terrane. Therefore, we can
304 infer that most of the natural fractures with a dip azimuth of $110\pm 20^\circ$ in the CCSD borehole
305 are developed in the subduction and exhumation process of the Sulu terrane. In addition, the
306 evolution of the nearby NNE-striking Tan-Lu fault could affect the development of the
307 natural fractures in the CCSD borehole too and probably generate some high dip angle
308 fractures with NNE-striking.

309 **5. Conclusion**

310 Abundant high-quality resistivity and ultrasonic image logs were obtained from the
311 CCSD borehole. These data have been analysed in order to recognise breakouts (BOs) and

312 drilling induced tensile fractures (DITFs) as well as natural fractures. Furthermore, the
313 azimuthal orientation (θ_{SH}) of the maximum horizontal principal stress (S_H) has been
314 computed using the BO and DITF information.

315 There was no discernible difference in the azimuthal orientation (θ_{SH}) of the S_H when
316 computed by using borehole BO data or by using DITF data. It has confirmed that there was
317 no statistically significantly difference by subjecting the 2 datasets to a t-test (at a level of
318 significance of 0.05). The mean value for the azimuth direction of the S_H is $\theta_{SH}=79.2\pm 17.4^\circ$.
319 This value is consistent with existing data on the World Stress Map and it is concluded that
320 the present orientation of S_H in the study area is dominated by the E-W collision between the
321 Pacific Plate and the Eurasian Plate.

322 Analysis of DITFs has indicated that there probably exists a critical well deviation angle,
323 below which ADITFs mainly occur and above which TDITFs occur. In the case of the CCSD
324 borehole, ADITFs occur in the upper section (0-2300 m) of the borehole whose dipping angle
325 is less than 10° , while TDITFs occur in the lower section (3800-5000 m) of the borehole
326 whose dipping angle is larger than 10° .

327 The magnitude relationship ($S_H > S_V > S_h$) of the three principal stresses indicates that the
328 regional stress field around the CCSD borehole is in a strike slip regime.

329 The depth intervals (e.g. 1180-1220 m, 2200-2300 m) with very high fracture frequency
330 occur in paragneiss and orthogneiss whose density and uniaxial failure strength are lower than
331 the other rocks in the CCSD borehole, so the failure strength should be a very important
332 factor that affects fracture frequency. Furthermore, the fracture frequency of the 0-3000 m
333 interval is greater than that of the 3600-5000 m interval, so the depth could be a potential

334 factor that affects fracture frequency.

335 The dip azimuth of natural fractures in the well ranges mainly between 90 to 180° in the
336 0-5000 m interval and is consistent with the dip azimuth of foliation observed in the core by
337 other researchers (Xu et al., 2009). We infer that the natural fractures and the foliation both
338 developed in response to the subduction and exhumation of the Sulu terrane and the
339 development of foliations affects the development of natural fractures greatly.

340 **Acknowledgements**

341 This study was supported by the National Natural Science Foundation of China (No.
342 41574121, 41104080) and the China Scholarship Council. Thanks to the CCSD project center
343 for providing well log and core data. We acknowledge the editors and reviewers for their
344 constructive suggestions and comments.

345

346

347 **References**

348 Aadnøy, B.S., Bell, J.S., 1998. Classification of drilling-induced fractures and their
349 relationship to in-situ stress directions. *The Log Analyst*, 39, 27–42.

350 Ames, L., Zhou, G., Xiong, B., 1996. Geochronology and Isotopic Character of
351 Ultrahigh-Pressure Metamorphism with Implications for Collision of the Sino-Korean
352 and Yangtze Cratons, Central China. *Tectonics*, 15, 472–489.

353 Anderson, E.M., 1951. *The Dynamics of Faulting and Dyke Formation with Applications to*
354 *Britain*, 2nd Ed, Oliver and Boyd, Edinburgh, pp.10-22.

355 Bell, J.S., Gough, D.I., 1979. Northeast-southwest compressive stress in Alberta—evidence

356 from oil wells. *Earth and Planetary Sciences Letters*, 45, 475-482.

357 Blumling, P., Fuchs, K., Schneider, T., 1983. Orientation of the stress field from breakouts in a
358 crystalline well in a seismic active area. *Physics of the Earth and Planetary Interiors*, 33,
359 250-254.

360 Brudy, M., Zoback, M.D. 1999. Drilling-induced tensile wall fractures: implications for
361 determination of in-situ stress orientation and magnitude. *International Journal of Rock*
362 *Mechanics and Mining Sciences*, 36, 191-215.

363 Cui, J., Wang, L., Li, P., Tang, Z., Sun, D., 2009. Wellbore breakouts of the main borehole of
364 Chinese Continental Scientific Drilling (CCSD) and determination of the present tectonic
365 stress state. *Tectonophysics*, 475, 220-225

366 Davies, R.J., Mathias, S.A., Moss, J., Hustoft, S., Newport, L., 2012. Hydraulic fractures:
367 how far can they go? *Marine and Petroleum Geology*, 37 (1), 1-6.

368 Deng, Y., Fan, W., Zhang, Z., Badal, J., 2013. Geophysical evidence on segmentation of the
369 Tancheng-Lujiang fault and its implications on the lithosphere evolution in East China.
370 *Journal of Asian Earth Sciences*, 78, 263-276

371 Ekstrom, M. P., Dahan, C., Chen, M. Y., Lloyd, P., and Rossi, D. J., 1987. Formation imaging
372 with microelectrical scanning arrays. *Log Analyst*, 28, 294-306.

373 Feng, C., Zhang, P., Qi, B., Meng, J., Tan, C., Hu, G., 2017. Recent Tectonic Stress Field at
374 the Shallow Earth's Crust near the Tan-Lu Fault Zone. *Geoscience*, 31(1): 46-68 (in
375 Chinese with English abstract).

376 Gaillot, P., Brewer, T., Pezard, P., Yeh, E.C., 2007. Technical Developments Borehole
377 Imaging Tools - Principles and Applications. *Scientific Drilling* 5, 1-4.

378 Glover, P., Bormann, P., 2007. The characterization of trough and planar cross-bedding from
379 borehole image logs. *Journal of Applied Geophysics*, 62, 178–191.

380 Goodman, H. E., Connolly, P., 2007. Reconciling subsurface uncertainty with the appropriate
381 well design using the mechanical Earth model (MEM) approach. *The Leading Edge*, 26,
382 585–588.

383 Gough, D.I., Bell, J.S., 1982. Stress orientations from oil-well fractures with examples from
384 Colorado, east Texas, and northern Canada. *Canadian Journal of Earth Sciences*, 19,
385 1358-1370.

386 Hacker, B. R., Ratschbacher, L., Webb, L., Ireland, T., Walker, D., Dong, S., 1998. U/Pb
387 zircon ages constrain the architecture of the ultrahigh-pressure Qinling–Dabie Orogen,
388 China. *Earth and Planetary Science Letters*, 161, 215–230.

389 Haimson, B.C. and Fairhurst, C., 1967, Initiation and extension of hydraulic fractures in rocks.
390 *Society of Petroleum Engineering Journal* 7, 310-318.

391 Haimson, B. C. and C. G. Herrick. 1986. Borehole breakouts — a new tool for estimating
392 In-Situ stress? *Proc., Int. Symp. on Rock Stress and Rock Measurements*, Stockholm,
393 A.A. Balkema, 271-278.

394 Heidbach, O., Rajabi, M., Reiter, K., Ziegler, M., WSM-Team, 2016. World Stress Map
395 Database Release 2016. GFZ Data Services. <http://doi.org/10.5880/WSM.2016.001>.

396 Hickman, S.H., Healy, J.H., Zoback, M.D., 1985. In situ stress, natural fracture distribution,
397 and borehole elongation in the Auburn Geothermal Well, Auburn, New York. *Journal of*
398 *Geophysics Research*, 90, 5497–5512.

399 Kimura, H., Kasahara, K., Takeda, T., 2009. Subduction process of the Philippine Sea Plate

400 off the Kanto district, central Japan, as revealed by plate structure and repeating
401 earthquakes. *Tectonophysics*, 472, 18-27

402 Liu, F. L., Xu, Z. Q., Xue, H. M., 2004. Tracing the Protolith, UHP Metamorphism, and
403 Exhumation Ages of Orthogneiss from the SW Sulu Terrane (Eastern China): SHRIMP
404 U-Pb Dating of Mineral Inclusion-Bearing Zircons. *Lithos*, 78, 411–429.

405 Liu, F. L., Xu, Z. Q., Liou, J.G., Dong, H.L., Xue, H. M., 2007. Ultrahigh-Pressure Mineral
406 Assemblages in Zircons from the Surface to 5158 m Depth in Cores of the Main Drill
407 Hole, Chinese Continental Scientific Drilling Project, Southwestern Sulu Belt, China.
408 *International Geology Review*, 49, 454-478.

409 Massiot, C., Celerier, B., Doan, M.-L., Little, T.A., McNamara, D.D., Townend, J., Schmitt,
410 D.R., Williams, J., Toy, V.G., Sutherland, R., Janku-Capova, L., Upton, P., and Pezard,
411 P., 2018. The Alpine Fault hangingwall viewed from within: structural analysis of
412 acoustic image logs in the DFDP-2B borehole, New Zealand. *Geochemistry, Geophysics,*
413 *Geosystems*, doi 2017GC007368.

414 Maxwell, S.C., Zimmer, U., Gusek, R.W., Quirk, D.J., 2009. Evidence of a Horizontal
415 Hydraulic Fracture From Stress Rotations Across a Thrust Fault. *SPE Production &*
416 *Operations*, 24, 312-319.

417 Nie, X., Zou, C., Pan, L., Huang, Z., Liu, D., 2013. Fracture analysis and determination of
418 in-situ stress direction from resistivity and acoustic image logs and core data in the
419 Wenchuan Earthquake Fault Scientific Drilling Borehole-2 (50-1370 m). *Tectonophysics*,
420 593, 161-171.

421 Nelson, E.J., Meyer, J.J., Hillis, R.R., Mildren, S.D., 2005. Transverse drilling-induced tensile

422 fractures in the West Tuna area, Gippsland Basin, Australia: implications for the in situ
423 stress regime. *International Journal of Rock Mechanics & Mining Sciences*, 42, 361-371.

424 Okey, A. I., Xu, S. T., Sengor, A. M. C., 1989. Coesite from the Dabie Shan Eclogites,
425 Central China. *European Journal of Mineralogy*, 1, 595–598.

426 Plumb, R.A., Hickman, S.H., 1985. Stress-induced borehole elongation: a comparison
427 between the four-arm dipmeter and the borehole televiewer in the Auburn geothermal
428 well. *Journal of Geophysical Research*, 90, 5513-5521.

429 Rajabi, M., Sherkati, S., Bohloli, B., Tingay, M., 2010. Subsurface fracture analysis and
430 determination of in-situ stress direction using FMI logs: an example from the Santonian
431 carbonates (Ilam Formation) in the Abadan Plain, Iran. *Tectonophysics*, 492, 192-200.

432 Rajabi, M., Tingay, M., Heidbach, O., Hillis, R., Reynolds, S., 2017. The present-day stress
433 field of Australia. *Earth Science Review* 168, 165-189.

434 Rider, M.H., 1996. *The Geological Interpretation of Wireline Logs*. Whittles Publishing,
435 Dunbeath.

436 Rowley, D. B., Xue, F., Tucker, R. D., Peng, Z. X., Baker, J., Davis, A., 1997. Ages of
437 Ultrahigh-Pressure Metamorphism and Protolith Orthogneisses from the Eastern
438 Dabieshan: U-Pb Zircon Geochronology. *Earth and Planetary Science Letters*, 151,
439 191–203

440 Sandiford, M., 2003. Neotectonics of southeastern Australia: linking the quaternary faulting
441 record with seismicity and in situ stress. *Geological Society of Australia Special
442 Publication*, 22, 101–113.

443 Serra, O., 2008. *Well Logging Handbook*. Paris, France, pp. 526-528.

444 Schlumberger, Ltd., 1994. FMI Fullbore Formation MicroImager: Houston, Texas
445 (Schlumberger Educational Services), pp. 3-5.

446 Schmitt, D. R., Currie, C., Zhang, L., 2012. Crustal stress determination from boreholes and
447 rock cores: Fundamental principles. *Tectonophysics*, 580, 1–26.

448 Schmitt, D. R., Haimson, B. C., 2016. Hydraulic Fracturing Stress Measurements in Deep
449 Holes, Chapter 6, in *Rock Mechanics and Engineering*, Vol. 1, ed., X-T. Feng, CRC
450 Press, 183-225

451 Sibson, R., Ghisetti, F., Ristau, J., 2011. Stress control of an evolving strike-slip fault system
452 during the 2010–2011 Canterbury, New Zealand, earthquake sequence. *Seismological
453 Research Letters*, 82 (6), 824–832.

454 Stein, R.S., 1999. The role of stress transfer in earthquake occurrence. *Nature*, 402 (6762),
455 605–609.

456 Stephen, M., 2009. *Essentials of Geology*. W.W. Norton & Co., New York.

457 Tingay, M., Reinecker, J., Müller, B., 2008. Borehole breakout and drilling-induced fracture
458 analysis from image logs. *World Stress Map Project Stress Analysis Guidelines*.
459 Available online at: www.world-stress-map.org.

460 Tingay, M., Hillis, R.R., Morley, C.K., King, R.C., Swarbrick, E., Damit, A.R., 2009.
461 Present-day stress and neotectonics of Brunei: implications for petroleum exploration
462 and production. *AAPG Bulletin*, 93, 75–100.

463 Vernik, L., Zoback, M.D., 1992. Estimation of the maximum horizontal principal stress
464 magnitude from stress-induced wellbore breakouts in the Cajon Pass scientific research
465 borehole. *Journal of Geophysical Research*, 97, 5109–5120.

466 Wan, T.F., Zhu, H., Zhao, L., Lin, J.P., Chen, J., Chen, J., 1996. Formation and evolution of
467 the Tancheng-Lujiag fault zone: a review. *Geoscience*, 10 (2), 159–168 (in Chinese with
468 English abstract).

469 Wang, X. M., Liou, J. G., Mao, H. K., 1989. Coesite-Bearing Eclogite from the Dabie
470 Mountains, Central China. *Geology*, 17, 1085–1088.

471 Wu, H.Y., Ma, K.F., Zoback, M., Boness, N., Ito, H., Hung, J.H., Hickman, S., 2007. Stress
472 orientations of Taiwan Chelungpu-fault Drilling Project (TCDO) hole-A as observed
473 from geophysical logs. *Geophysical Research Letter*, 34, L01303.

474 Xu, S. T., Okay, A. I., Ji, S., 1992. Diamond from Dabie Shan Metamorphic Rocks and Its
475 Implication for Tectonic Setting. *Science*, 256, 80–82

476 Xu, Z.Q., Wang, Q., Tang, Z.M., Chen, F.Y., 2009. Fabric kinematics of the ultrahigh
477 pressure metamorphic rocks from the main borehole of the Chinese Continental
478 Scientific Drilling Project: implications for continental subduction and exhumation.
479 *Tectonophysics*, 475, 235–250

480 Zhang, J., Lang, J., Standifird, W., 2009. Stress, porosity, and failure dependent
481 compressional and shear velocity ratio and its application to wellbore stability. *Journal of*
482 *Petroleum Science and Engineering*, 69, 193–202.

483 Zhang, J., 2013. Borehole stability analysis accounting for anisotropies in drilling to weak
484 bedding planes. *International Journal of Rock Mechanics and Mining Sciences*, 60,
485 160–170.

486 Zhang, R. Y., Hirajima, T., Banno, S., Cong, B., Liou, J.G., 1995. Petrology of
487 Ultrahigh-Pressure Rocks from the Southern Su-Lu Region, Eastern China. *Journal of*

488 Metamorphic Geology, 13, 659–675

489 Zhang, Z. M., Shen, K., Xiao, Y. L., Hosfs, J., Liou, J.G., 2006. Mineral and fluid inclusions
490 in zircon of UHP metamorphic rocks from the CCSD-main drill hole: a Record of
491 metamorphism and fluid activity. *Lithos*, 92,378–398

492 Zhou, H., Ding, R., 1995. Study of the characteristics of crustal stress field in East China by
493 inversion of nodal-plane data. *Tectonophysics*, 245(1-2), 53-59

494 Zhu, G., Wang, D.X., Liu, G.S., Niu, M.L., Song, C.Z., 2004. Evolution of the Tan-Lu fault
495 zone and its responses to plate movement in west Pacific basin. *Chinese Journal of
496 Geology*, 39 (1), 36-49 (in Chinese with English abstract).

497 Zoback, M.D., Moos, D., Mastin, L., Andersson, R.N., 1985. Well bore breakouts and in-situ
498 stress. *Journal of Geophysical Research*, 90, 5523–5530.

499 Zoback, M.D., Barton, C.A, Brudy, M., Castillo, D.A., Finkbeiner, T., Grollimund, B.R.,
500 Moos, D.B., Peska, P., Ward, C.D., Wiprut, D.J., 2003. Determination of stress
501 orientation and magnitude in deep wells. *International Journal of Rock Mechanics and
502 Mining Sciences*, 40, 1049–1076.

503 Zoback, M. D., 2007. *Reservoir geomechanics*. Cambridge University Press, Cambridge, pp.
504 242-249.

505

506

507

508 **Figure captions**

509 **Fig. 1.** Preferential orientation of breakout and drilling induced tensile fracture (DITF)
510 relative to the direction of the maximum horizontal principal stress in a vertical borehole (S_H :
511 the maximum horizontal stress; S_h : the minimum horizontal stress) (modified after [Rider,](#)
512 [1996](#); [Hillis and Reynolds, 2000](#); [Morin and Wilkens, 2005](#); [Schmitt et al., 2012](#)). (a)
513 Horizontal cross-section of the borehole, (b) unrolled image of the borehole wall.

514

515 **Fig. 2.** Location of the CCSD borehole and its adjacent tectonic environment background.
516 The inset shows the regional location with respect to nearby plate boundaries. (UHPM:
517 Ultra-high pressure and metamorphic; YQWF: Yantai-Qingdao-Wulian Fault; JXF:
518 Jiangshan-Xiangshui Fault; EU: Eurasian Plate; NA: North America Plate; PA: Pacific Plate;
519 PH: Philippine Sea Plate; red arrows indicate the moving direction of the plate relative to the
520 EU) (modified after [Zhang et al. \(2006\)](#) and [Kimura et al. \(2009\)](#))

521

522 **Fig. 3.** Some conventional logs and a simplified lithology profile of the CCSD borehole. (a)
523 Gamma ray log (RG), (b) density log (DEN), (c) acoustic velocity log (V_p), (d) deep
524 resistivity log (RD), (e) caliper log (CAL). (The lithology profile is modified from [Liu et al.](#)
525 [\(2007\)](#) and [Xu et al. \(2009\)](#)). (The CAL log is very unstable and increased greatly in the
526 3000-3600 m interval due to the borehole enlargement operation).

527

528 **Fig. 4.** Identifying breakouts, drilling induced tensile fractures and nature fractures by
529 Formation Micro-resistivity Image (FMI) and Ultra-Sonic (amplitude) Image (USI) logs from
530 the CCSD borehole. (a) Borehole breakout (BO), (b) axial drilling induced tensile fracture
531 (ADITF) and nature fracture (NF), (c) transverse drilling induced tensile fracture (TDITF).
532 (Image logs are displayed unrolled clockwise and oriented to the geographic north.)

533

534 **Fig. 5.** An example of natural fracture features appearing on the Formation Micro-Resistivity
535 Image (FMI) and Ultra-Sonic (amplitude) Image (USI) logs between 231 and 233 m of the
536 CCSD borehole, together with relevant core image projected into azimuthal coordinates.
537 (Image logs are displayed unrolled clockwise and oriented to the geographic north)

538

539 **Fig. 6.** An example of foliation and natural fracture (NF) features appearing on the Formation
540 Micro-Resistivity Image (FMI) and Ultra-Sonic (amplitude) Image (USI) logs between 457
541 and 460 m of the CCSD borehole, together with relevant core image projected into azimuthal
542 coordinates. Foliations appear more frequently on the resistivity image logs and display lots
543 of fine and parallel stripes. Natural Fractures usually appear as dark (low-resistivity)
544 quasi-sinusoidal stripes on both the resistivity and ultrasonic image logs and maybe parallel to
545 the foliations.

546

547 **Fig. 7.** (a) The orientation of BO versus depth, (b) the orientations of ADITF and TDITF
548 versus depth, (c) the direction of the S_H derived from the orientations of BO, ADITF and
549 TDITF, (d) the dip azimuth of the CCSD borehole, (e) the deviation of the CCSD borehole, (f)
550 the magnitudes of S_V , S_H and S_h versus depth (reused the magnitude data of S_H and S_h
551 published by [Cui et al. \(2009\)](#) with permission granted by Elsevier). The rose diagram in
552 panel (a), (b) and (c) showed the sample numbers and statistical features of the azimuth data
553 set. (No useful image logs are recorded in the 3000-3600 m interval due to the borehole
554 enlargement operation)

555

556 **Fig. 8.** Orientation of the present-day maximum horizontal principal stress in eastern China
557 from the World Stress Map database ([Heidbach et al., 2016](#)) and from the CCSD borehole.
558 (NF=normal faulting stress regime; SS=strike-slip faulting stress regime; TF=thrust faulting
559 stress regime; U=undefined stress regime; Quality A=the direction of S_H is within $\pm 15^\circ$;
560 Quality B=the direction of S_H is within $\pm 20^\circ$; Quality C=the direction of S_H is within $\pm 25^\circ$).

561

562 **Fig. 9.** Fracture dip azimuth (θ_{in}) and frequency versus the depth of the borehole. (a) Dip
563 azimuth for individual fractures, (b) fracture density in numbers of fractures per 10 meters

564 interval, (c) simplified lithology profile (modified from [Liu et al. \(2007\)](#) and [Xu et al. \(2009\)](#)).
565 (no useful image logs are recorded in the 3000-3600 m interval due to the borehole
566 enlargement operation)

567

568 **Fig. 10.** Rose diagrams of the dip azimuth of the natural fractures for different depth intervals
569 (please note that image data are missing in the depth interval 3000-3600 m and cannot be
570 analyzed). (a) 28-736 m; (b) 736-1113 m; (c) 1113-1596 m; (d) 1596-2038 m; (e) 2038-2280
571 m; (f) 2280-2920 m; (g) 3623-5000 m; (h) 28-5000 m.

572

573 **Fig. 11.** Rose diagrams of the dip azimuth of the foliations for different depth intervals (from
574 [Xu et al. \(2009\)](#) with permission to reprint granted by Elsevier). (a) 0-736 m; (b) 736-1113 m;
575 (c) 1113-1596 m; (d) 1596-2038 m; (e) 2038-2280 m; (f) 2280-2920 m; (g) 2920-3225 m; (h)
576 3225-5158 m.

577

578

579

580 **Table captions**

581

582 **Table 1**

583 Lithological unit (modified from [Xu et al. \(2009\)](#) with permission to reprint granted by
584 Elsevier) and dip azimuth of fractures and foliations in each unit.

585

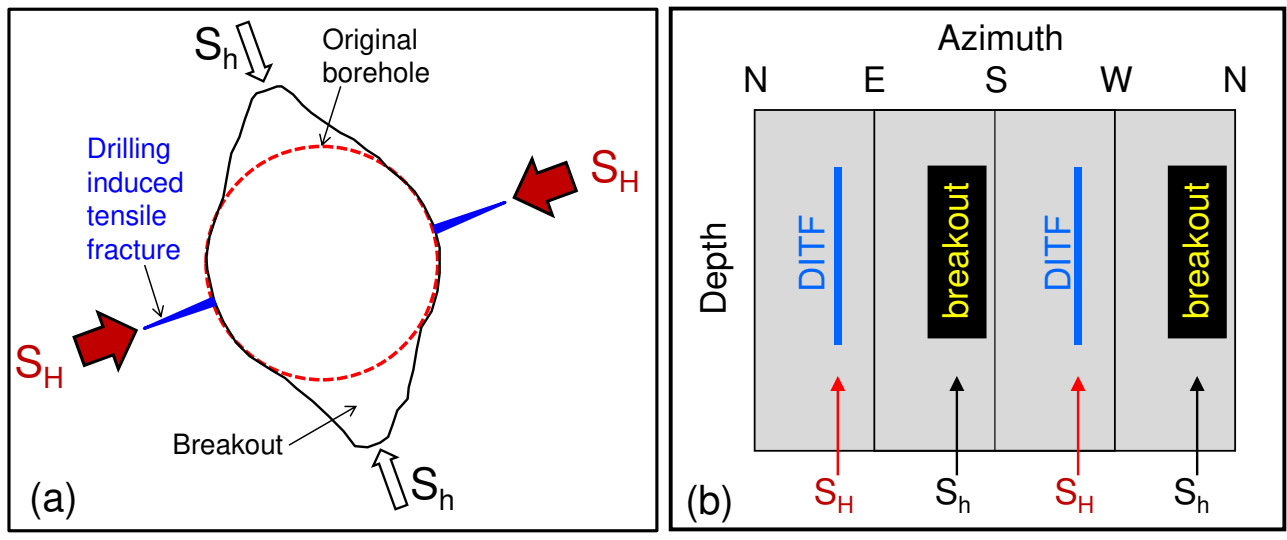


Fig. 1

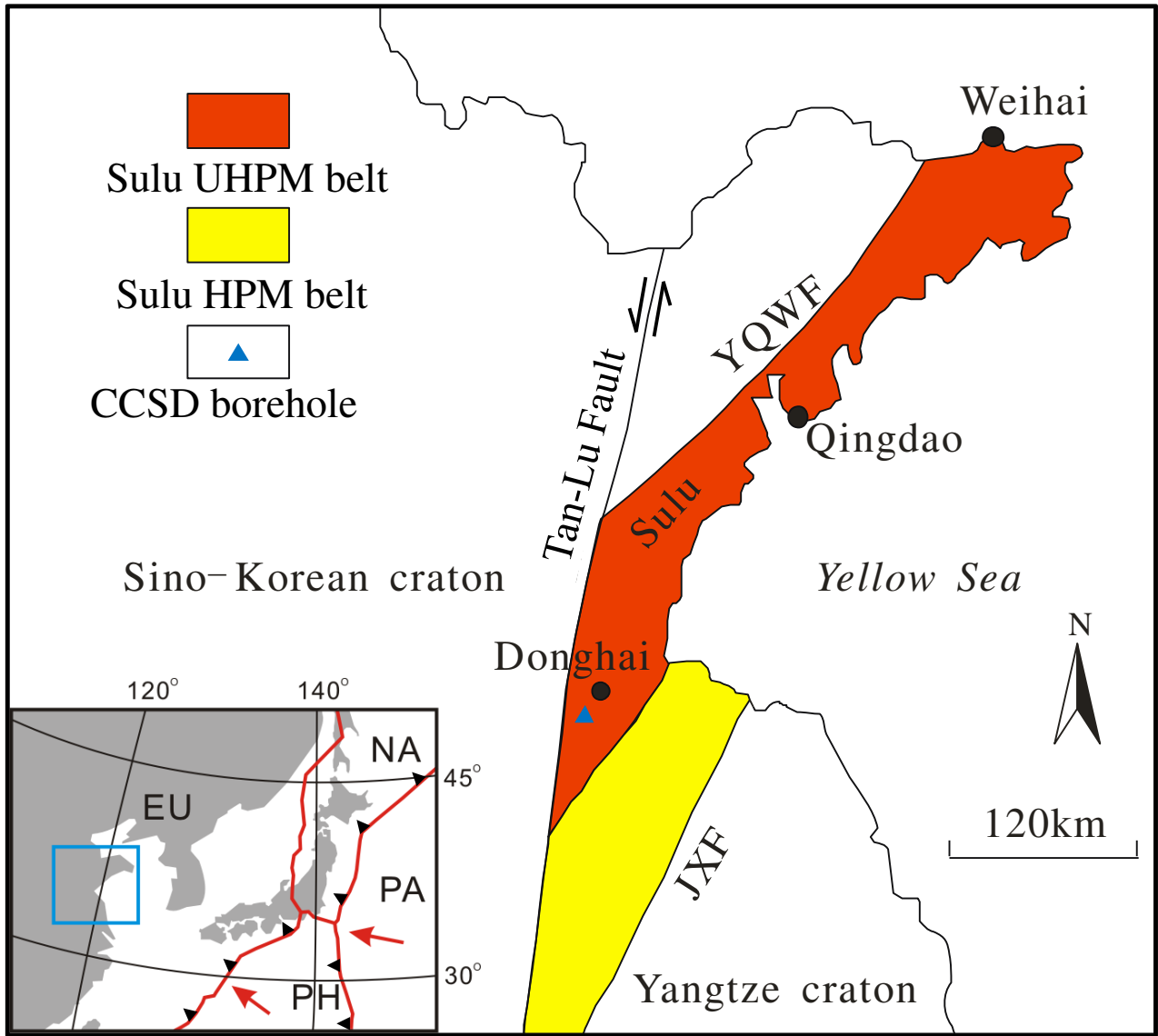


Fig. 2

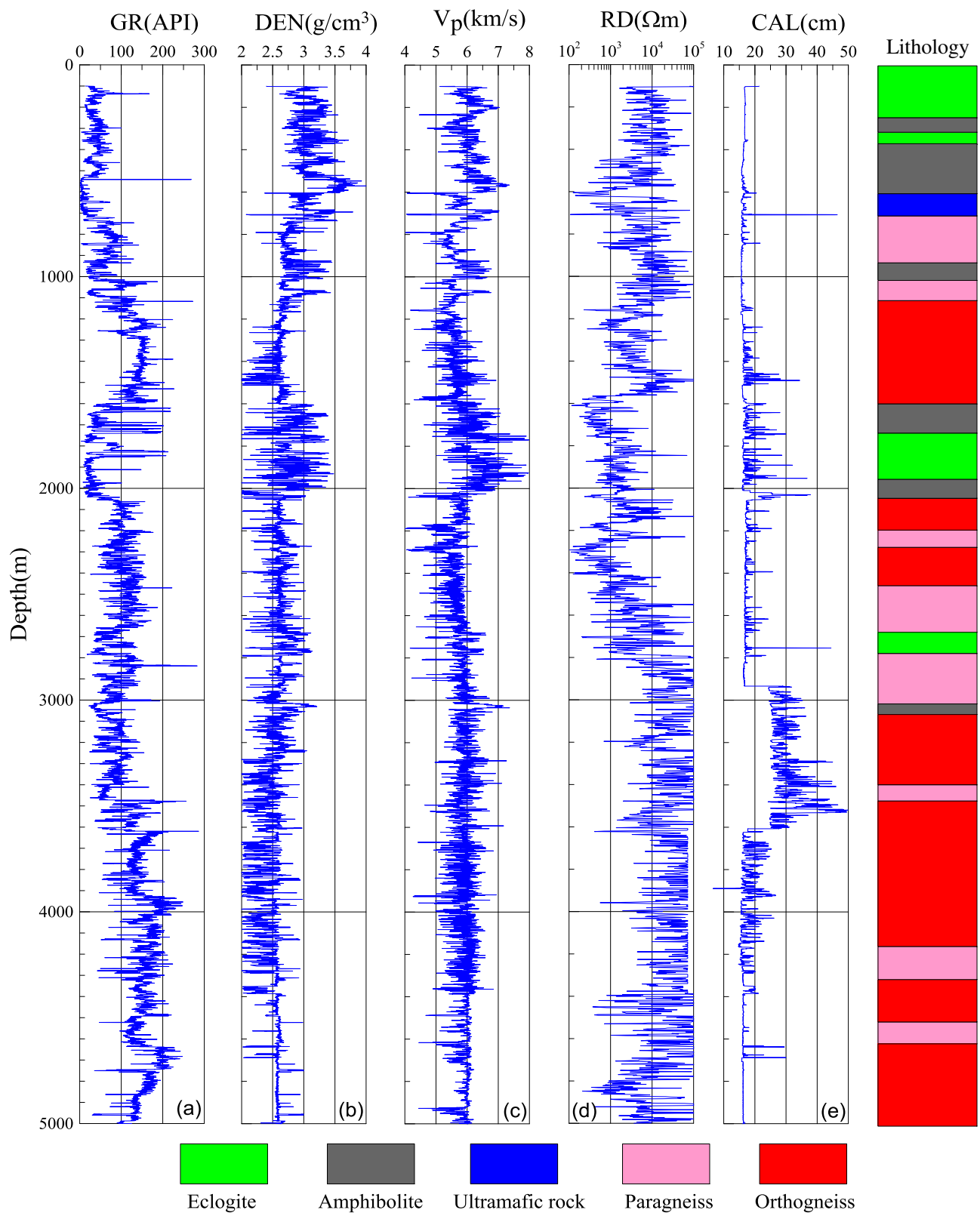


Fig. 3

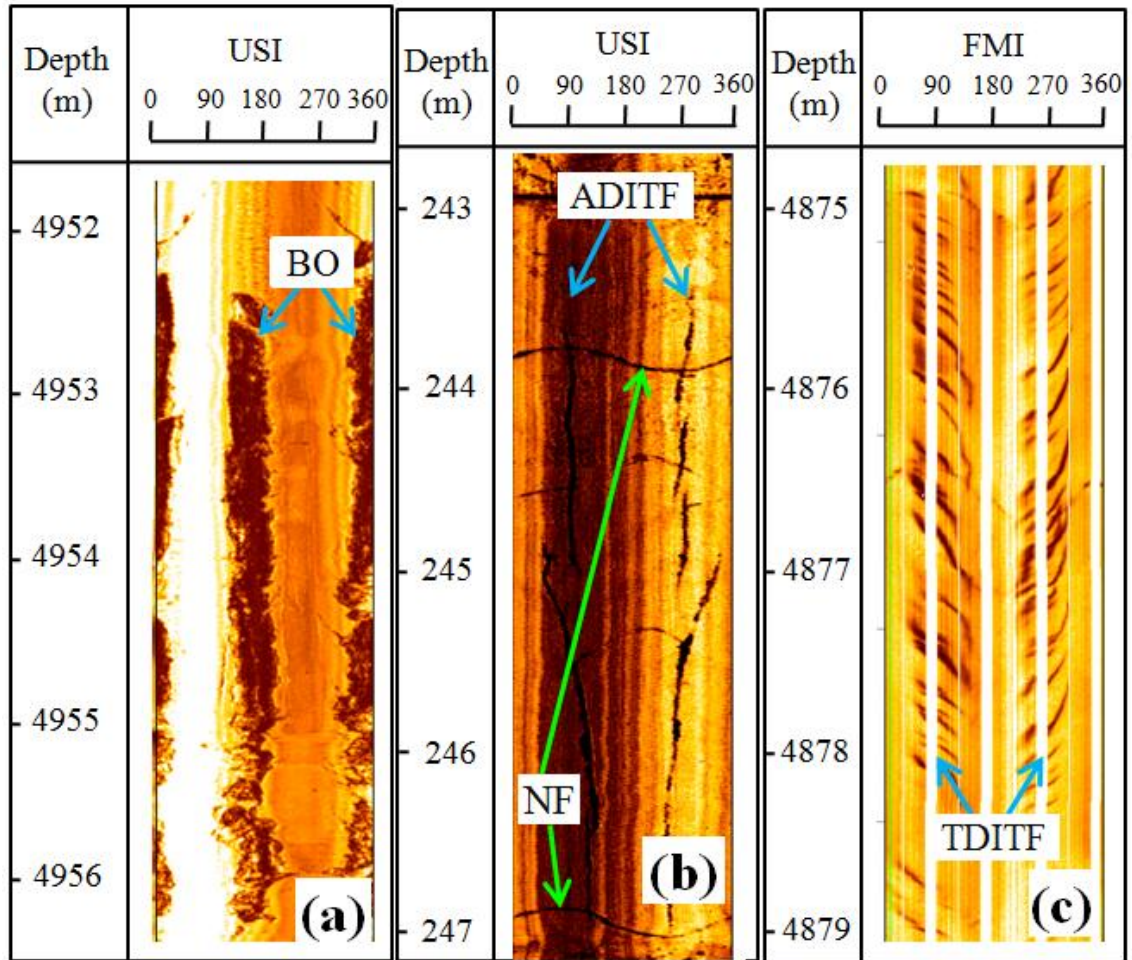


Fig. 4

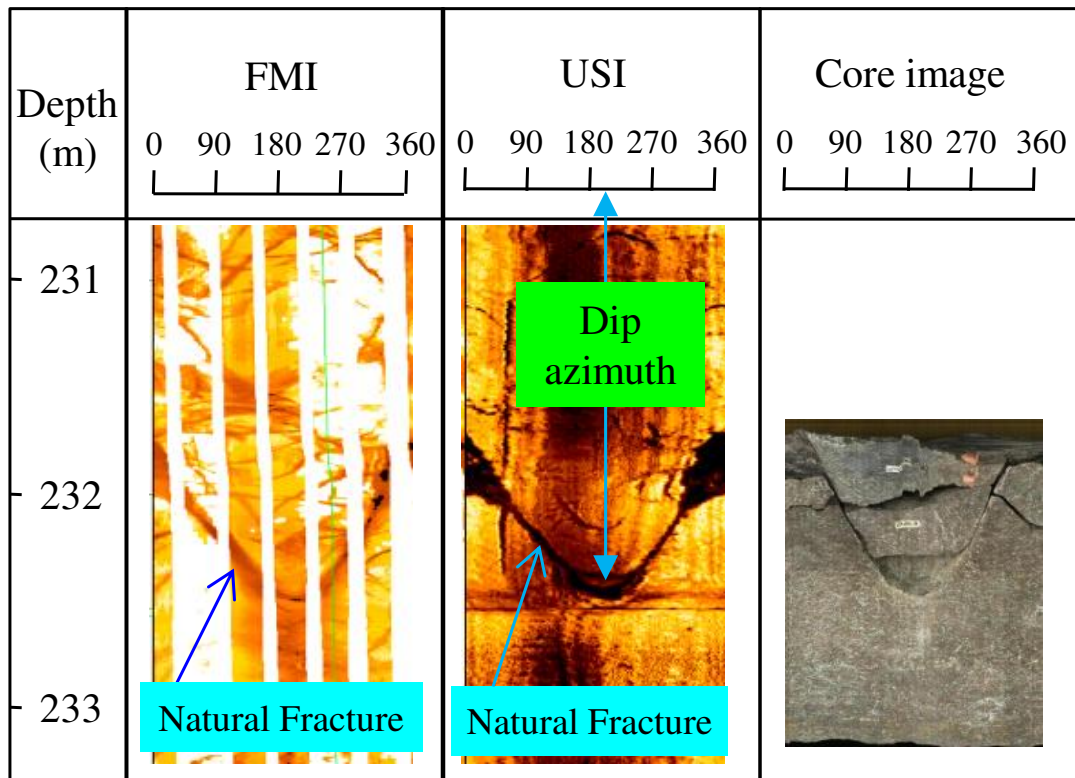


Fig. 5

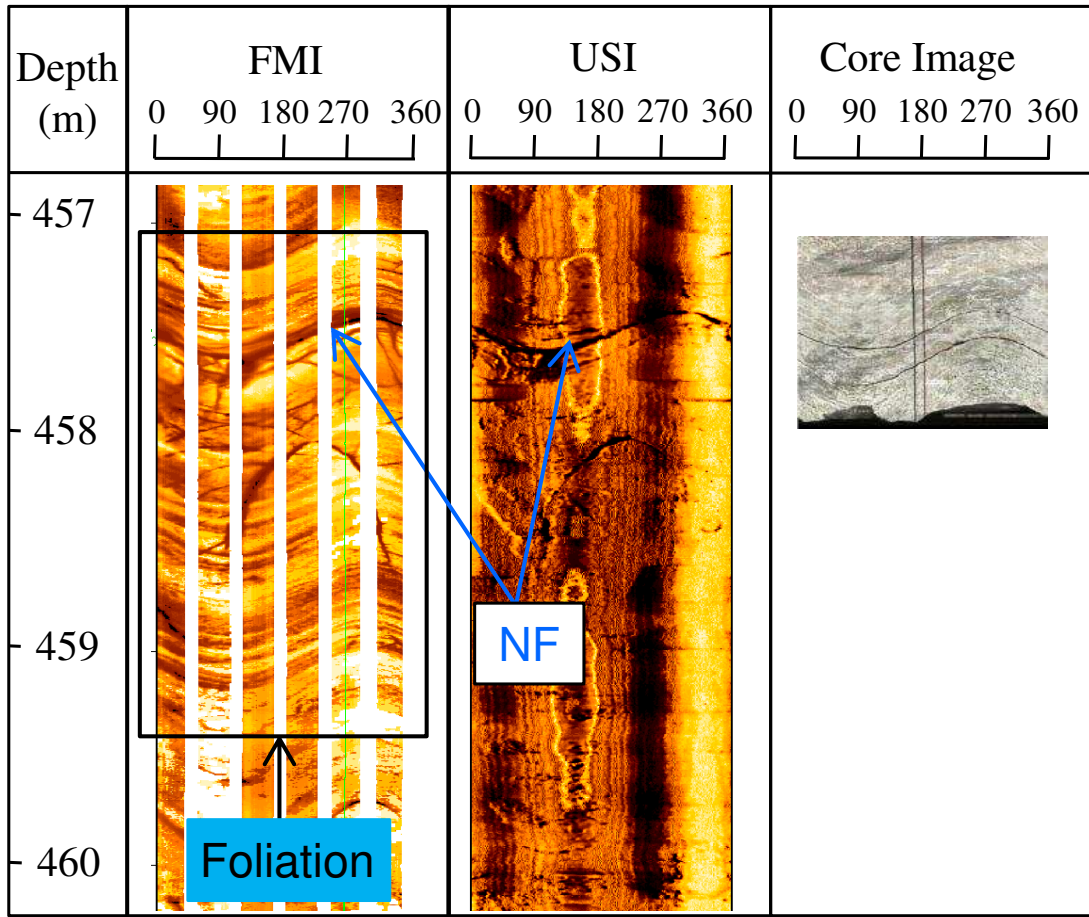


Fig. 6

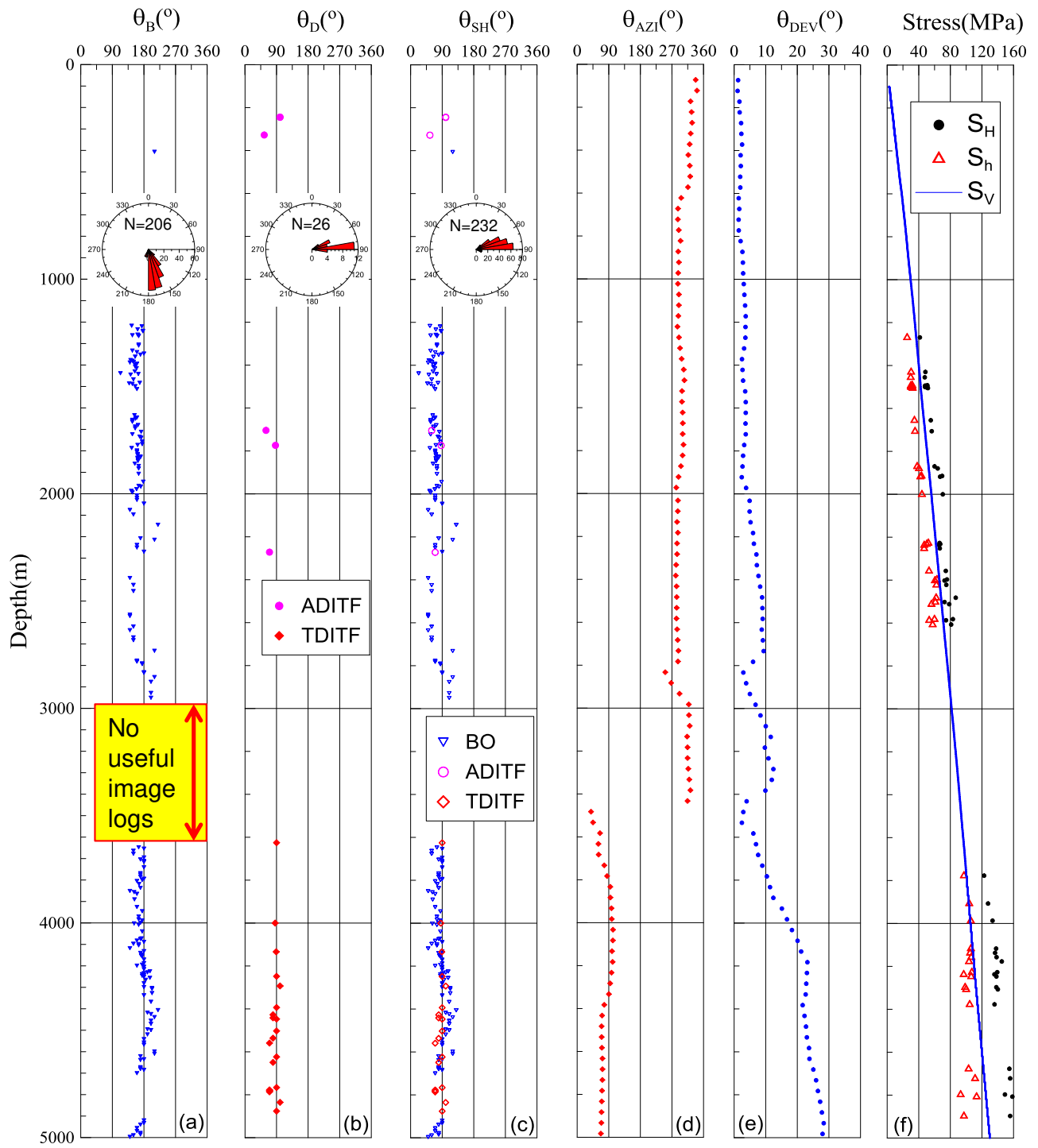


Fig. 7

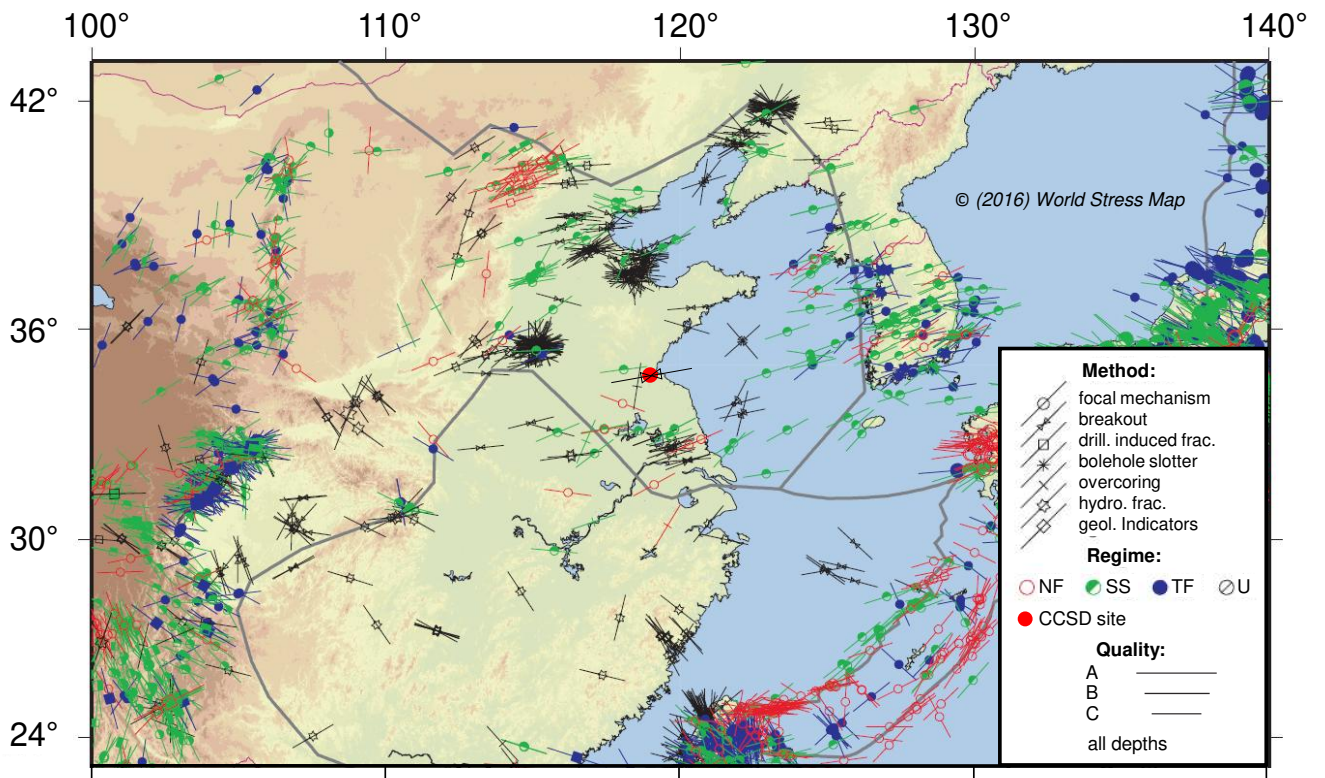


Fig. 8

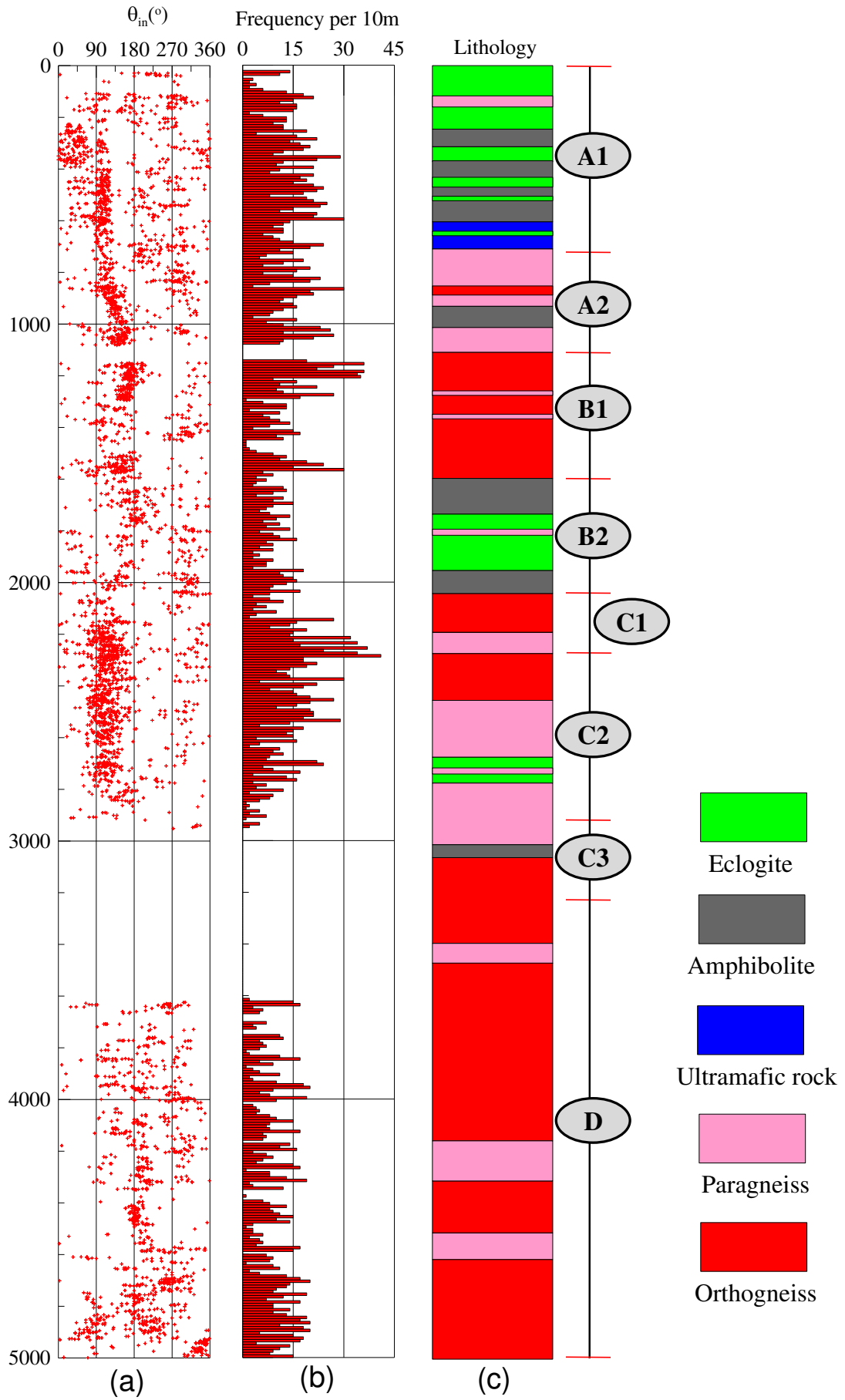


Fig. 9

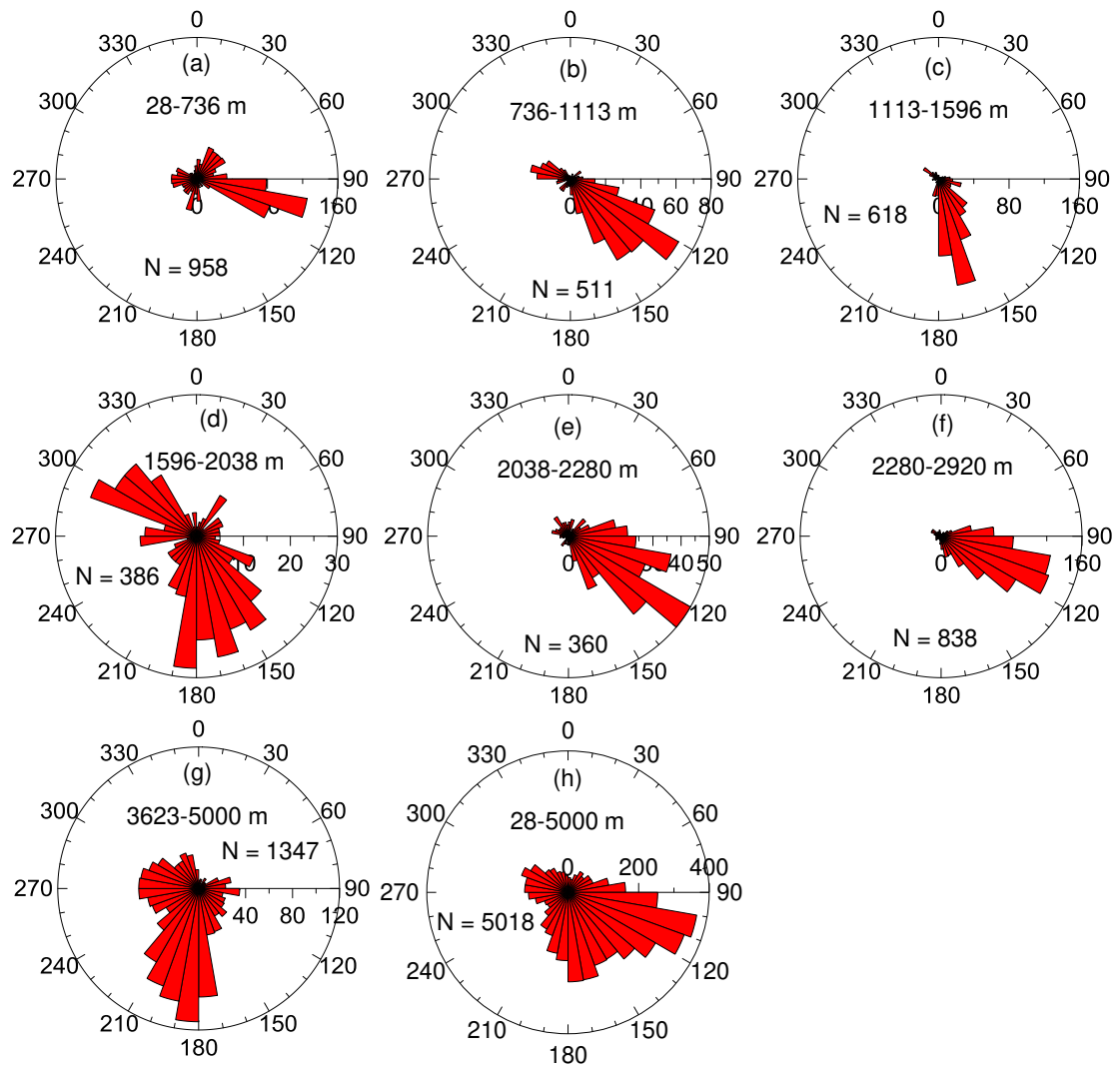


Fig. 10

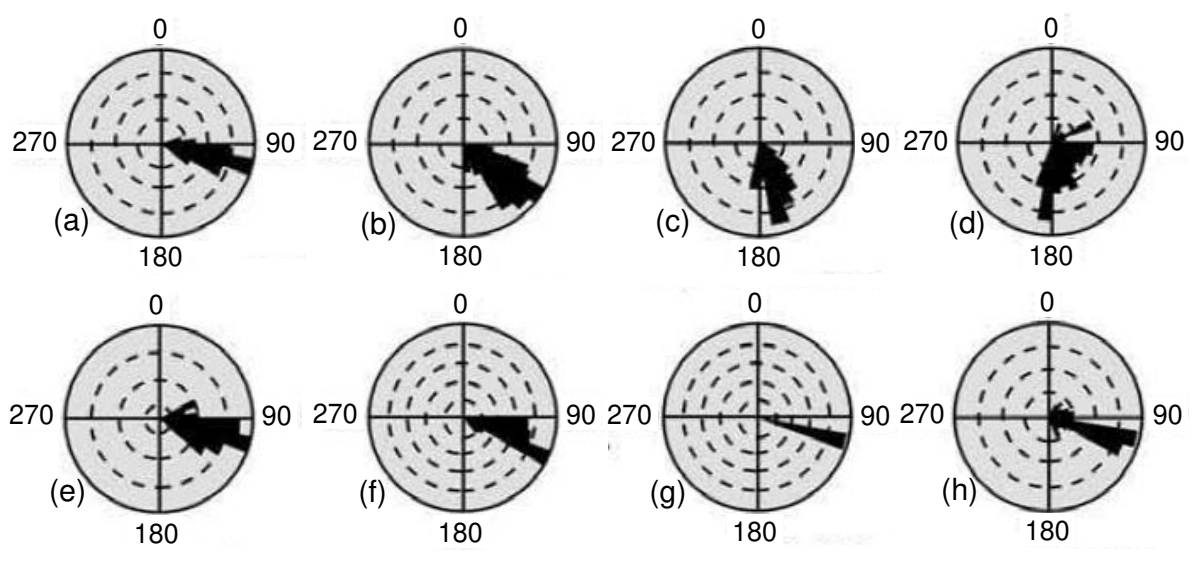


Fig. 11

Table 1

Unit	Depth (m)	Lithology	Fig. 10	Dip direction of fractures	Fig. 11	Dip direction of foliations
A1	0-736	eclogite	(a)	110±10°	(a)	110±10°
A2	736-1113	paragneiss	(b)	130±20°	(b)	135±10°
B1	1113-1596	orthogneiss	(c)	165±10°	(c)	160±10°
B2	1596-2038	eclogite	(d)	165±20°	(d)	180±15°
C1	2038-2280	orthogneiss	(e)	120±20°	(e)	110±10°
C2	2280-2920	paragneiss	(f)	110±15°	(f)	110±5°
C3	2920-3225	paragneiss and orthogneiss	-	-	(g)	105±5°
D	3225-5158	orthogneiss and paragneiss	(g)	200±20°	(h)	110±10°

